Portable setup for Bell test with entangled photons

Alejandro Jaramillo

Supervised by: José María Gómez Cama and Bruno Juliá-Díaz

Facultad de Física UB (ICCUB), 08028 Barcelona

28th August 2022

In this thesis we build and characterize a portable experimental setup to perform a Bell test using the CHSH Bell inequality with polarization-entangled photons. These photons are produced using Type-I Spontaneous Parametric Down-Conversion with two BBO crystals. We study the theory behind the CHSH Bell inequality, and the mechanism of Spontaneous Parametric Down-Conversion and compare a Hidden Variable Theory to Quantum Theory.

Contents

Alejandro Jaramillo: ajarampa7@alumnes.ub.edu

Acknowledgements

This work has been partially funded by Grant No. PID2020-114626GB-I00 from the MICIN/AEI/10.13039/501100011033 and by the Facultat de Fisica of the University of Barcelona. We thank Prof. Jordi Mompart, Marti Pedemonte, Robert Benassai, and Morgan Mitchell for their help at various stages of the project.

We thank to Martí Duocastella and his team, Andrea and Pietro, for their support with material and guidance.

We thank also to the team of Proto&Go!, Eksma Optics and the Facultat de Física workshop people for their help and insight on mechanics.

Finally, special thanks to my tutors, José María Gómez Cama and Bruno Juliá-Díaz for their dedication on this project.

1 Introduction

In the last decades, Quantum Technologies have become of upmost importance. Applications like Quantum Computing and Quantum Communications promise to accelerate technological development [ABB+18]. One of the most purely Quantum phenomena we make use of to realize such technologies is entanglement. For this reason, it is necessary to find ways of producing entangled systems we can easily reproduce and experiment on. However, the microscopic nature of entanglement makes it difficult to assess whether what we are producing are entangled systems or not. Hence, we also need an experiment that can discriminate Quantum correlations from correlations that can be explained with classical − thus, less exploitable − theories. That kind of experiment is called a Bell test.

Our objective in this thesis is to build a compact and portable experimental realization of a Bell test with polarization-entangled photons produced using Type-I Spontaneous Parametric Down-Conversion (SPDC). First, we provide a historical and theoretical background to Bell inequalities and compare a Hidden Variable Theory to Quantum Theory. Then, we provide a brief insight into the mechanism of Type-I SPDC. Finally, we describe the experimental setup and present the obtained results.

1.1 Bell's inequalities. The CHSH Bell's inequality

At the beginning of the 20th century, as a result of many phenomena that could not be explained with (now called) classical theories, the Quantum Mechanical description of reality was born. It introduced many new concepts − such as the quantization of energy or the wave function formalism − and a notion of a non-deterministic reality. Quantum Mechanics provides an effective mathematical description to problems such as the black body radiation problem [Pla00] and the photoelectric effect [Ein05]. However, this theory fails to give a physical meaning to many of its components. Furthermore, the mathematics of Quantum Mechanics allows certain phenomena that are not allowed within classical theories. In particular, one of the most unintuitive of those is entanglement. From a classical point of view, entanglement allows the properties of a system to entirely depend on the actions performed on another non-causally-correlated system. This breaks a well-established rule of the universe: locality.

In this context, Einstein, Podolski and Rosen − EPR for short − wrote in 1935 the paper "Can Quantum-Mechanical Description of Physical Reality Be Considered Complete?" [EPR35]. There they discussed what they thought to be the conditions every theory should fulfill in order to be considered natural and satisfactory. The two concepts of discussion were Completeness and Reality. The first one, as quoted from the original paper, requires that *"Every element of the physical reality must have a counterpart in physical theory"*. That is, there must be a one-to-one correspondence between the elements we include and use in our physical theory and the elements of the reality they are describing. The Reality condition asks that *"If, without in any way disturbing a system, we can predict with certainty (i.e., with probability equal to unity) the value of a physical quantity, then there exists an element of physical reality corresponding lo this physical quantity"*. This last requirement attacks the non-commutability of operators in the Quantum Theory: two measurements of the same quantity q of a system performed before and after a measurement of another, non-compatible quantity p can yield different results, implying that q and p cannot have simultaneous reality. They argue then that if Quantum Mechanics is a local and real theory it cannot be complete, and state that they believe that such a theory (local, real and complete) is indeed possible.

This remained a matter of quasi-philosophical debate for almost 30 years until John

Bell published his paper "On the Einstein Podolsky Rosen Paradox" [Bel64]. In that paper, Bell provided a series of mathematical conditions (the so-called Bell inequalities) that any local and real theory should fulfill. Those conditions, when experimentally implemented, constitute what is known as a Bell test.

A Bell scenario is conformed by two space-like separated parties A and B (Alice and Bob) that receive a pair of correlated systems from a source. Alice (Bob) can perform α (β) $= 1, ..., m$ different measurements with a (b) $= 1, ..., r$ possible outcomes. By conducting a series of measurements and computing the frequency of each result, the parties could construct the probability distribution $p(a, b|\alpha, \beta)$. Since the experiments performed by Alice and Bob are space-like separated, the results on each end can only depend on the local measurements and the state of the system. This state can be codified in a variable λ (it can take any form, but the particular form of λ does not change any of the derivations, so for simplicity we use a scalar to represent it). Thus, a local probability distribution in this scenario must be of the form [Bel64]

$$p(\alpha, \beta|a, b) = \int D_A(a|\alpha, \lambda) D_B(b|\beta, \lambda) \rho(\lambda) d\lambda, \tag{1}$$

where $\rho(\lambda)$ represents the probability distribution of the preparation variable λ and $D_A(a|\alpha, \lambda)$ and $D_B(b|\beta, \lambda)$ are deterministic functions (i.e. can only take the values 0 and 1). This imposes the Reality requirement. Note that we have not specified the form of the underlying theory, so this applies to any local and real theory as described by EPR.

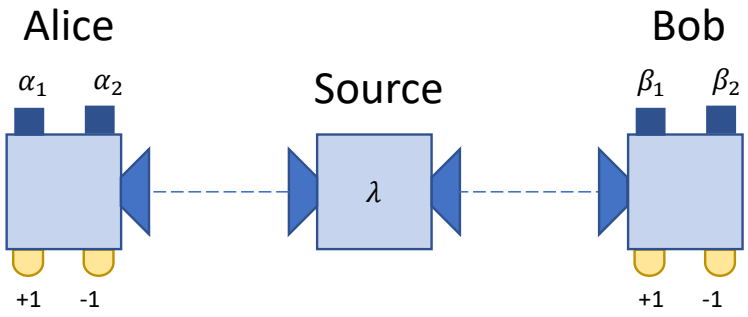

Figure 1: Schematic representation of the CHSH Bell scenario. Alice and Bob receive a pair of systems with a preparation λ. They perform two possible measurements in a black box-like device by pressing the blue buttons. A light under the box indicates the result of the measurement.

The simplest case of a Bell scenario is realized when reducing the number of possible measurements and outcomes to just two. It is described in a paper by J. Clauser, M. Horne, A. Shimony and A. Holt in 1969 [CHSH69] and is illustrated in Fig. 1. This scenario yields an inequality that can be derived in just a few lines: the CHSH inequality. For mathematical simplicity, we impose the possible results of both party's measurements to be equal to ± 1. Let us introduce the quantity

$$S = a(\alpha_1, \lambda)b(\beta_1, \lambda) + a(\alpha_1, \lambda)b(\beta_2, \lambda) + a(\alpha_2, \lambda)b(\beta_1, \lambda) - a(\alpha_2, \lambda)b(\beta_2, \lambda), \tag{2}$$

where a (b) is the results of performing the α (β) measurement. This quantity can be understood as a measurement of the correlations between the systems. Since the probability

distribution of both a and b are deterministic given α, β and γ, we can perform a series of manipulations to proof that the absolute value of S is bounded by 2.

$$\begin{aligned} |S| &= |a(\alpha_1,\lambda)b(\beta_1,\lambda) + a(\alpha_1,\lambda)b(\beta_2,\lambda) + a(\alpha_2,\lambda)b(\beta_1,\lambda) - a(\alpha_2,\lambda)b(\beta_2,\lambda)| \\ &= |a(\alpha_1,\lambda)\left[b(\beta_1,\lambda) + b(\beta_2,\lambda)\right] + a(\alpha_2,\lambda)\left[b(\beta_1,\lambda) - b(\beta_2,\lambda)\right]|. \end{aligned} \tag{3}$$

Since $b = \pm 1$, either the $b(\beta_1,\lambda) + b(\beta_2,\lambda)$ or the $b(\beta_1,\lambda) - b(\beta_2,\lambda)$ term cancels and the other term takes a value of ± 2. Thus, since $a = \pm 1$ as well, then we can state

$$|S| = 2 \rightarrow S = \pm 2. \tag{4}$$

And finally, it is easy to see that

$$|\,\langle S\rangle\,| \leq 2. \tag{5}$$

Eq. (5) is known as the CHSH inequality. This inequality presents a limit for S for any set of measures in any possible local and real theory. However, it is violated by Quantum Mechanics. It was proved by Cirel'son [Cir80] that the maximum value this inequality can take in Quantum Mechanics is $2\sqrt{2}$. The maximum mathematical value that S can take is 4. This is the limit to the so-called No-Signaling correlations. These three sets are represented in Fig. 2. It is interesting to note that part of the Quantum ($\mathcal{Q}$) and the No-Signaling ($\mathcal{NS}$) sets lie under the Bell inequality limiting hyperplane. This shows that there are some elements out of the local set that cannot be detected by a Bell's inequality. From this we can conclude that a Bell test is an effective way of discriminating the nature of an experiment – i.e., determining if it can be explained with a local and real theory or if a different type of theory is needed. Note that a violation of a Bell inequality does not otherwise imply the veracity of Quantum Theory, nor its fulfillment rejects it.

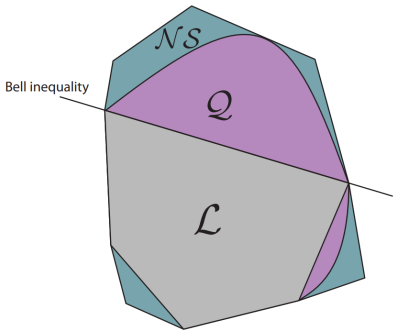

Figure 2: Sketch of the No-Signaling ($\mathcal{NS}$), Quantum ($\mathcal{Q}$), and local ($\mathcal{L}$) sets. Notice the strict inclusions $\mathcal{L} \in \mathcal{Q} \in \mathcal{NS}$. The hyperplanes delimiting the set $\mathcal{L}$ correspond to Bell inequalities. Image taken from Ref. [BCP+14].

In the Quantum formalism, the observable S has an associated operator of the form

$$\hat{S} = \hat{A}_1 \otimes \hat{B}_1 + \hat{A}_1 \otimes \hat{B}_2 + \hat{A}_2 \otimes \hat{B}_1 - \hat{A}_2 \otimes \hat{B}_2. \tag{6}$$

The maximum violation of the CHSH Bell inequality can be obtained with the state of Eq. (7) and the set of observables in Eq. (8).

$$|\Psi\rangle = \frac{|00\rangle + |11\rangle}{\sqrt{2}}. \tag{7}$$

$$\begin{aligned} \hat{A}_1 = \hat{\sigma}_x, \quad \hat{A}_2 = \hat{\sigma}_z, \\ \hat{B}_1 = \frac{\hat{\sigma}_x + \hat{\sigma}_z}{\sqrt{2}}, \quad \hat{B}_1 = \frac{\hat{\sigma}_x - \hat{\sigma}_z}{\sqrt{2}}. \end{aligned} \tag{8}$$

These state and observables can be experimentally implemented in a number of ways, the most common of which is using polarization-entangled photons. It is also simple, since laser sources and linear polarizers are standard lab equipment that can be found easily.

1.2 The CHSH inequality with polarization-entangled photons

As indicated in section 1.1, to perform a CHSH Bell test we need a source of correlated systems and a set of measures with outputs ± 1. Since we are interested in studying polarization-entangled photons, polarization is the physical property we measured for this experiment. The measure of the polarization is done by setting two detection systems − A and B, one for each photon − consisting on a polarizer at an angle α (β) from the vertical and a Single Photon Counting Module (SPCM). For a fixed position of a polarizer at an angle γ, we assign the value $+1$ to the photon going through and being detected (we call this V_γ) and -1 to the photon going through the polarizer rotated 90° from its original position (H_γ). The possible combinations are $V_\alpha V_\beta$, $V_\alpha H_\beta$, $H_\alpha V_\beta$ and $H_\alpha H_\beta$. The first and the latter events yield a combined result of $+1$ and the second and third yield -1. By choosing 2 angles for each polarizer, we can build the S quantity as described in Eq. (2).

The expectation value of S can be computed as follows. First, we define

$$E(\alpha, \beta) = \langle a(\alpha) b(\beta) \rangle \,, \tag{9}$$

where $a(\alpha)$ and $b(\beta)$ are the results of the measurements in detectors A and B. The expectation value of S is

$$\langle S \rangle = E(\alpha, \beta) + E(\alpha, \beta') + E(\alpha', \beta) - E(\alpha', \beta'), \tag{10}$$

$$E(\alpha, \beta) = P_{VV}(\alpha, \beta) - P_{VH}(\alpha, \beta) - P_{HV}(\alpha, \beta) + P_{HH}(\alpha, \beta), \tag{11}$$

where $P_{ij}(\alpha, \beta)$ is the probability of $i_\alpha j_\beta$ $(i, j = V, H)$ occurring. These probabilities can be computed by counting the coincidence detections at angles α, β, $\alpha_\perp$ and $\beta_\perp$.

$$P_{VV}(\alpha, \beta) = \frac{N(\alpha, \beta)}{N_{tot}(\alpha, \beta)}, \qquad P_{VH}(\alpha, \beta) = \frac{N(\alpha, \beta_\perp)}{N_{tot}(\alpha, \beta)}, \tag{12}$$

$$P_{HV}(\alpha, \beta) = \frac{N(\alpha_\perp, \beta)}{N_{tot}(\alpha, \beta)}, \qquad P_{HH}(\alpha, \beta) = \frac{N(\alpha_\perp, \beta_\perp)}{N_{tot}(\alpha, \beta)}, \tag{13}$$

where $N_{tot} = N(\alpha, \beta) + N(\alpha, \beta') + N(\alpha', \beta) + N(\alpha', \beta')$.

As discussed in Sec. 1.1, the maximal violation of the CHSH Bell inequality can be obtained with the state described in Eq. (7) and the set of observables in Eq. (8). This corresponds to a polarization state

$$|\psi\rangle = \frac{|VV\rangle + |HH\rangle}{\sqrt{2}}, \tag{14}$$

and a set of angles

$$\begin{aligned} \alpha = 0° \quad \alpha' = 45° \\ \beta = 22.5° \quad \beta' = -22.5°. \end{aligned} \tag{15}$$

These angles correspond to a transformation $2\pi \to \pi$ from the set of operators given in Eq. (8) due to the 180° periodicity of polarization.

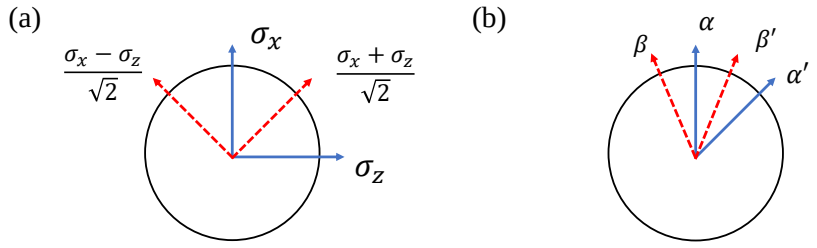

Figure 3: Sketch of the angles needed for maximal violation of CHSH Bell's inequality. Blue continuous arrows for Alice's operators, red dashed arrows for Bob's operators. (a) Configuration of the Quantum operators. (b) Configuration of the polarizers angles.

1.3 A Hidden Variable Theory

A Hidden Variable Theory (HVT) is a theory that attempts to explain the results of a Quantum experiment by adding new, non-contemplated – hidden – variables. These kind of theories can be ruled out by a Bell test, since they are bounded by classical limits as the one in Eq. (5). In 2002, D. Dehlinger and M. W. Mitchell published two papers [DM02a, DM02b] where they described a setup like the one on this thesis. They also briefly discussed a reasonable HVT that could get close to the Quantum predictions. In Quantum Theory, the probability of a coincidence detection in directions α and β of a two photon system in the state $|\Psi\rangle$ is given by

$$p(\alpha, \beta) = |\langle \alpha, \beta | \Psi \rangle|^2, \tag{16}$$

where $|\alpha, \beta\rangle$ corresponds to a state with one photon polarized in α direction and one photon polarized in β. For the states that can be constructed with this setup, described in Eq. (30), this probability reads

$$p(\alpha, \beta) = \sin^2\alpha \sin^2\beta \cos^2\theta_l + \cos^2\alpha \cos^2\beta \sin^2\theta_l + \frac{1}{4}\sin 2\alpha \sin 2\beta \sin 2\theta_l \cos\phi. \tag{17}$$

For this HVT, we consider a source that produces pairs of photons polarized in a random direction λ. The probability of a photon going through a polarizer set at angle γ is

$$p_V^{(\mathrm{HVT})}(\gamma, \lambda) = \begin{cases} 1 & |\gamma - \lambda| \leqslant \pi/4 \\ 1 & |\gamma - \lambda| > 3\pi/4 \\ 0, & \text{otherwise.} \end{cases} \tag{18}$$

When considering coincidence detections, we need to compute the probability of a photon with polarization λ going through two polarizers set at angles α and β. This can be computed graphically by considering the overlap between two 90° sections centered at α, $\alpha + 180°$, β and $\beta + 180°$. The coincidence probabilities for HVT are

$$p_{VV}^{(HVT)} = p_{HH}^{(HVT)} = \frac{1}{2} - \frac{|\beta - \alpha|}{\pi}, \tag{19}$$

$$p_{VH}^{(HVT)} = p_{HV}^{(HVT)} = \frac{|\beta - \alpha|}{\pi}. \tag{20}$$

To compare this theory with the Quantum Theory, we programmed a simulation that computes S numerically from the individual probability of Eq. (18). The full code can be found in Appendix C. Plots for different configurations can be found in Fig. 4. As we expected, the HVT does not violate Bell's inequality. It actually presents a plateau right when it is about to surpass the classical limit for Eq. (15) configuration. We can see that the S curve computed with the HVT is not smooth and presents changes in its slope at $\beta' = \alpha, \alpha', \alpha + 90°, \alpha' + 90°$. This is due to changes in the curvature of the absolute values that constitute the individual probabilities. Maximum and minimum values of S also depend on the difference between α and α'. Maximum span is obtained when $\alpha' = \alpha + 45°$ Changes in β do not change the position of the curvature changing points, but displace the curve vertically. This is due to the fact that β and β' are never in one same absolute value element. It is interesting to see that the two curves can become similar at some regions. However, considering the overall discrepancies, we can state a clear incompatibility between both theories that would be easy to discriminate with experimental data.

1.4 Second-Harmonic Generation and Spontaneous Parametric Down-Conversion

Nonlinear optics studies the effects that arises when electromagnetic fields strongly modify the structure of the medium it is being transmitted through [Boy08]. Some of those phenomena are used to manipulate light in many different ways. One of such ways is the generation of entangled photons through a process called Parametric Down-Conversion. To better understand this process, let us briefly introduce some notions of the interactions between matter and strong EM fields.

The polarization of matter in linear optics depends linearly on the applied field as

$$P(t) = \epsilon_0 \chi^{(1)} E(t), \tag{21}$$

where ϵ_0 is the permitivity of free space and $\chi^{(1)}$ is known as the linear susceptibility of the medium. However, the relation between P and E can take different, more complex forms. This can be expressed by taking the power series of P as a function of E

$$\begin{aligned} P(t) &= \epsilon_0 \left[\chi^{(1)} E(t) + \chi^{(2)} E^2(t) + \chi^{(3)} E^3(t) + ... \right] \\ &= P^{(1)}(t) + P^{(2)}(t) + P^{(3)}(t) + ... \end{aligned} \tag{22}$$

where $\chi^{(2)}$ and $\chi^{(3)}$ are the second-order and third-order susceptibilities. These factors introduce new light-matter interactions. Let us consider an electric field of the form

$$E(t) = E e^{-i\omega t} + \text{c.c.}, \tag{23}$$

that is incident on a crystal with $\chi^{(2)} \neq 0$. Then the polarization of the crystal is

$$P^{(2)}(t) = 2\epsilon_0 \chi^{(2)} E E^* + \left(\epsilon_0 \chi^{(2)} E^2 e^{-i2\omega t} + \text{ c.c. } \right). \tag{24}$$

We see in Eq. (24) a term at zero frequency and a term at frequency 2ω. This last term is related to a process called second-harmonic generation. Second-Harmonic Generation (SHG) describes the production of photons at a frequency 2ω from an input beam at a frequency ω. It can be understood as the destruction of two photons of frequency ω and the simultaneous creation of a single photon of frequency 2ω through the excitation and

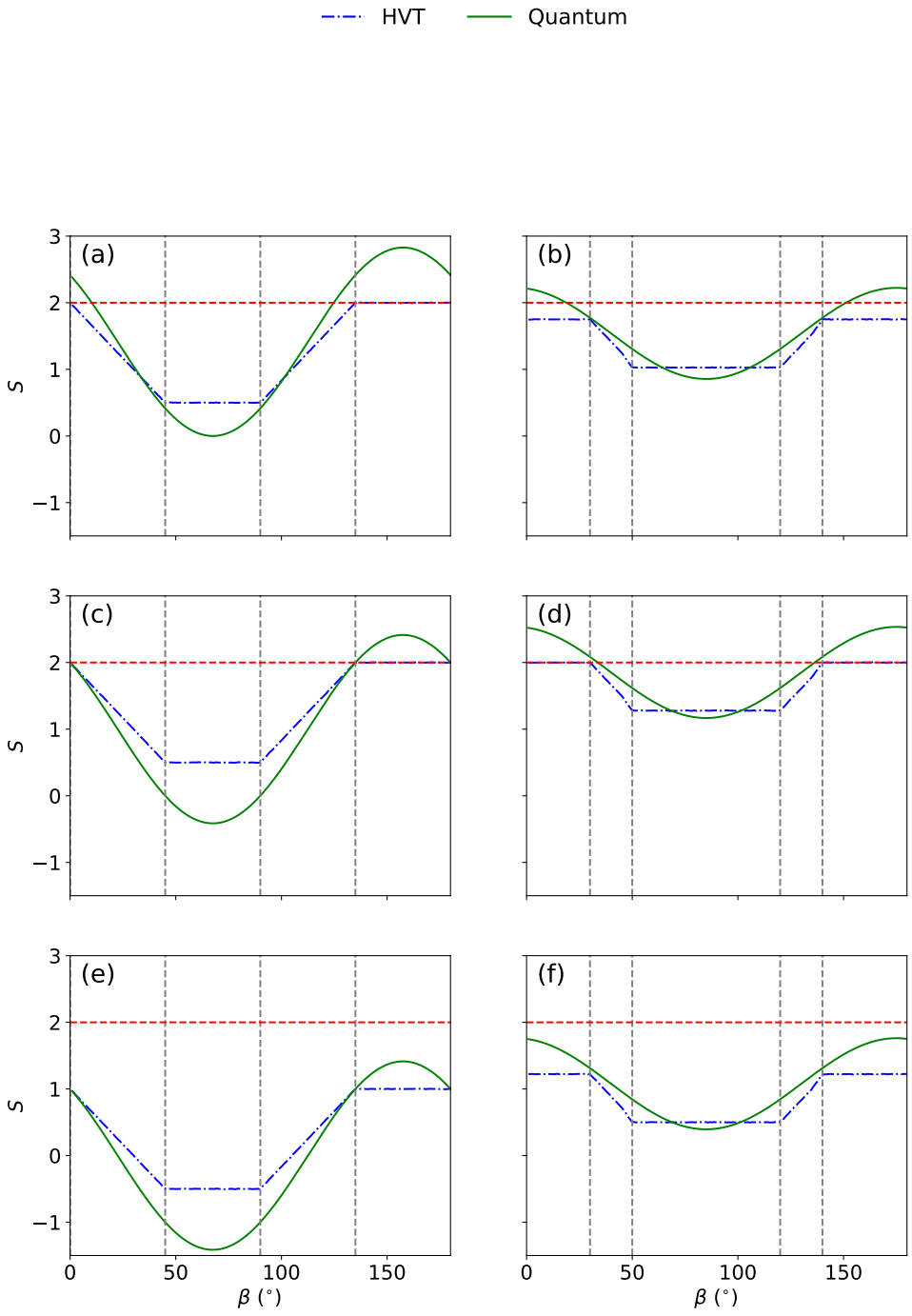

Figure 4: Comparison of the $S-\beta'$ curve for the HVT (dot-dashed blue line) and the Quantum prediction (continuous green line). Dashed grey lines mark $\beta' = \alpha, \alpha', \alpha + 90°, \alpha' + 90°$. Dashed red line marks the classical $S = 2$ limit. (a), (c) and (e): $\alpha = 0°$, $\alpha' = 45°$. (b), (d) and (f): $\alpha = 30°$, $\alpha' = 50°$. (a), (b): $\beta = 22.5°$. (c), (d): $\beta = 45°$. (e), (f): $\beta = 67.5°$.

de-excitation of a crystal ion into virtual energy levels represented by the dashed lines in Fig. 5.

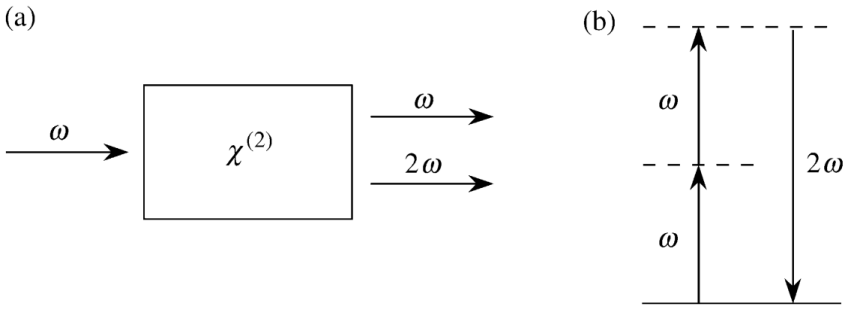

Figure 5: Sketch representation of Second-Harmonic Generation. (a) Geometry of the process. (b) Representation of the energy levels of the ion. The continuous line represents the real energy level. The dashed lines represent the virtual energy levels after the excitation. Image taken from Ref. [Boy08].

The efficiency of this process depends on a condition known as phase-matching. Let us introduce the phase missmatch Δk as

$$\Delta k = 2k_1 - k_2, \tag{25}$$

where k_1 is the wavevector of the incident field and k_2 is the wavevector of the resulting field. The maximum intensity of the outcoming beam is reached when the condition $\Delta k = 0$ is fulfilled, and rapidly decays as we move away from perfect phase-matching. Phase-matching depends on factors such as the structure of the crystal, the wavelength of the incident field and temperature [Boy08].

The time-reversed process of SHG is called Spontaneous Parametric Down-Conversion (SPDC). It is one of the most extended processes to produce polarization-entangled photons. In this process, a single photon interacts with the crystal, producing a pair of photons (called signal and idler) of half the frequency of the pump photons. The down-converted photons exit the crystal at a cone of aperture $2\theta_{wo}$ known as walkoff angle. Due to conservation of energy and momentum, these two photons have correlations in their polarization degree of freedom [KWW+99]. Depending on how the phase-matching condition is fulfilled, the down-converted photons can have the same polarization, which is perpendicular to that of the pump photons (called Type-I SPDC) or have perpendicular polarizations. In that way, a nonlinear crystal that supports SHG with Type-I phase-matching, can down-convert photons as

$$|\leftrightarrow\rangle \rightarrow |\updownarrow\rangle \otimes |\updownarrow\rangle\,, \tag{26}$$

where $|\leftrightarrow\rangle$ indicates a polarization state in an arbitrary direction and $|\updownarrow\rangle$ a polarization state perpendicular to the first one. It was proposed in 1999 [KWW+99] to use two Type-I nonlinear crystals – in particular, β-Barium Borate (BBO) crystals –, mounted face-to-face and rotated 90° to produce polarization-entangled photons. The pump photons can be down-converted in either crystal, since the crystals are indistinguishable [KWW+99]

$$|V\rangle \rightarrow |HH\rangle\,, \tag{27}$$

$$|H\rangle \rightarrow e^{i\Delta}\,|VV\rangle\,, \tag{28}$$

where Δ is a relative phase due to effects such as dispersion and birefrigence. This allows the creation of polarization-entangled states using linearly polarized light. To do so, one can send photons polarized an angle θ_l from the vertical through a birefringent crystal to obtain the state

$$|\psi_l\rangle = \cos\theta_l\,|V\rangle + e^{i\phi_l}\sin\theta_l\,|H\rangle\,, \tag{29}$$

where ϕ_l is the relative phase due to the birefringent crystal. By sending these photons into a set of crystals as the one mentioned above, we can obtain a polarization-entangled state

$$|\Psi\rangle = \cos\theta_l\,|HH\rangle + e^{i\phi}\sin\theta_l\,|VV\rangle\,, \tag{30}$$

where $\phi = \phi_l + \Delta$ is the total phase shift. By adequately choosing the angle of incidence of the pump photons in the birefringent crystal, we can correct the phase shift to obtain the desired state. In particular, when $\phi = 0$ and $\theta_l = 45°$, we obtain one of the so-called Bell states

$$|\Psi\rangle = \frac{|VV\rangle + |HH\rangle}{\sqrt{2}}, \tag{31}$$

which is the same as the one in Eq. (7). By adding additional optical elements, we can obtain any of the four Bell states.

Type-I SPDC has been found to have an efficiency of $\sim 10^{-6}$ – that is, one conversion per 10^6 incident photons [BLCB16]. It is one of the best entangled photon sources and is widely used to produce entanglement and run Bell tests in academia.

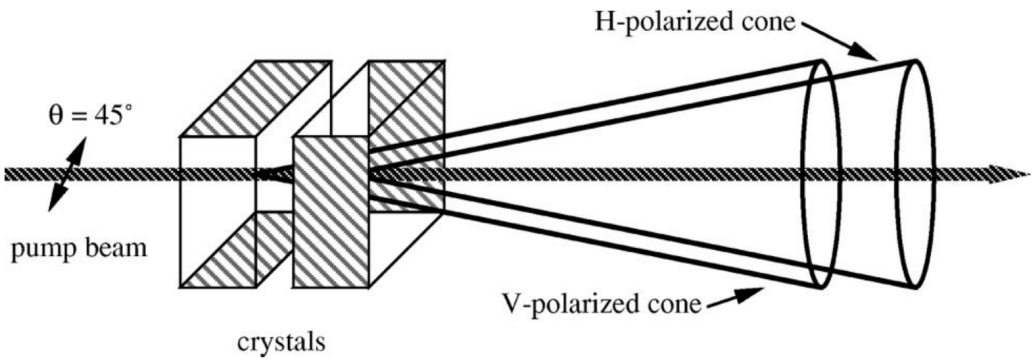

Figure 6: Representation of the entangled photon source. Image taken from Ref. [DM02b].

2 Experimental setup

There are many simple and easy to perform experiments that explore purely Quantum phenomena, but only a Bell test can discriminate whether classical theories are fit to explain a given experiment or not. For that reason, our objective was to construct a compact and portable realization of a Bell test that can be used to test different entangled photon sources for both advanced research and undergrad labs. This experiment is based on the apparatus designed by D. Dehlinger and M. W. Mitchell [DM02a, DM02b]. We aimed to use standard lab equipment that can be easily obtained through any optics material manufacturer. We used 405 nm laser light to produce 810 nm photons through Type-I SPDC with two BBO crystals cut at 44.3° and Single Photon Counting Modules connected to a coincidence detection circuit to count the number of coincidences at the desired angles of polarization. All the setup is build inside of a 90×60 cm box to achieve low-light conditions in a portable manner.

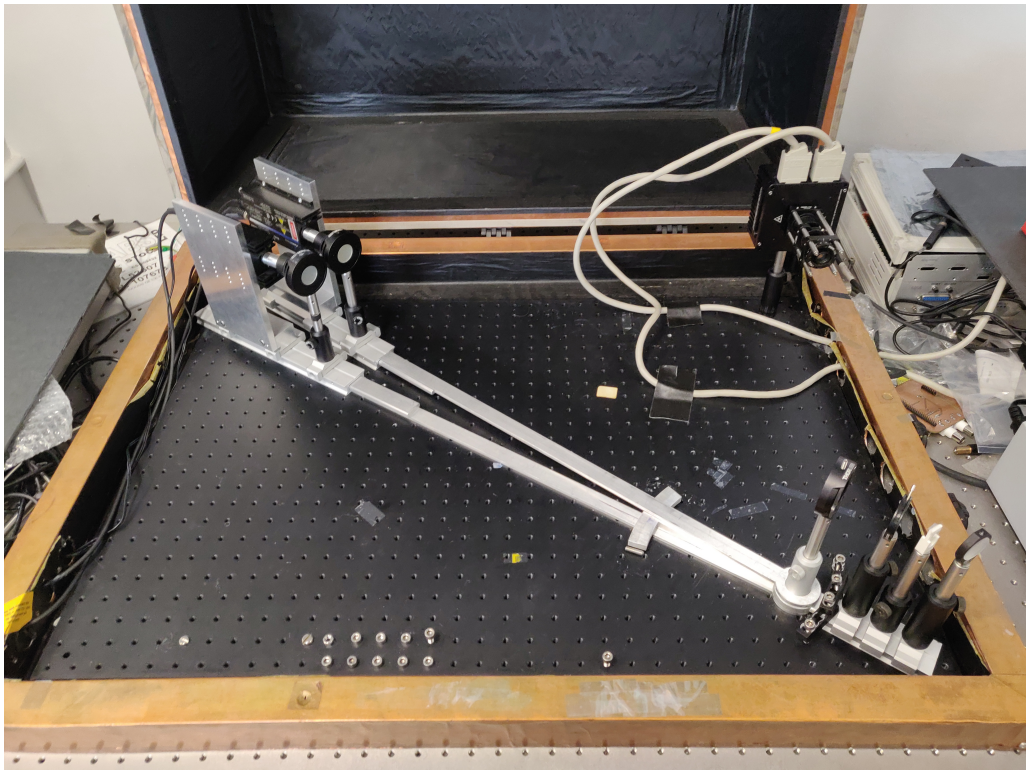

Figure 7: Photograph of the apparatus. From left to right: detection ensemble and its mechanical components, production ensemble, laser and its cage system.

2.1 Optics

The optical system is build on an optical breadboard inside of the 90×60 cm box. The box has its insides covered with black paper that reduces reflections and background light. It has a set of holes drilled on the sides to pass the necessary cables, after which are sealed using black electrical tape. This ensemble was tested to reduce noise from saturated Single Photon Counting Modules ($> 10^9$ counts per second) to less than 10^3 counts per second in a normally lit room. It, however, presents a limitation to the geometry of the setup, since all the optical elements need to fit inside of the box. Pictures of the final apparatus can be found in Fig. 7 and a sketch of the montage can be found in Fig. 8.

The setup can be divided into two parts: the photon production part and the photon detection part. The photon production part consists of a 405 nm B Pin Code Laser Diode in a temperature-controlled casing. The casing's front plate is equipped with tapped holes to mount a 30 mm cage system. This allows to place a focusing aspheric lens (f = 4.52 mm), a BG25 Colored Glass band-pass filter, an iris diaphragm and a polarizer in a rotation mount. The laser light then travels through free space and is reflected by a ∅1" broadband dielectric mirror into a 10x10x0.5 mm X-cut quartz crystal used to adjust the phase difference between the vertical and horizontal components. Finally, the photons reach two BBO crystals, rotated 90° with respect to each other. This allows the incoming photons to be downconverted in either crystal, producing − with the correct positioning of the quartz crystal − the desired state.

The photon detection part consists of two identical arms that rotate around the BBO crystal. Each arm is constituted by a linear polarizer (which acts as the "measurement button" in our Bell scenario), a RG-780 colored glass long-pass filter and a Single Photon Counting Module (model SPCM-AQR-12) which incorporates a focusing lens mounted on an aluminum tube. Due to one of the filters being damaged, it was substituted by a 800 nm centered band-pass filter with a band width of 40 nm. Since this filter has a narrower transmission band, it blocks more light than the long-pass filter, but the frequency of the down-converted photons − 810 nm − lies within the band, allowing the detection of said photons. The arms form an angle θ_A and θ_B with the beam. For maximum coincidence detections, these angles must be equal [DM02a], and at 2.7°, which is the walkoff angle indicated by the manufacturer.

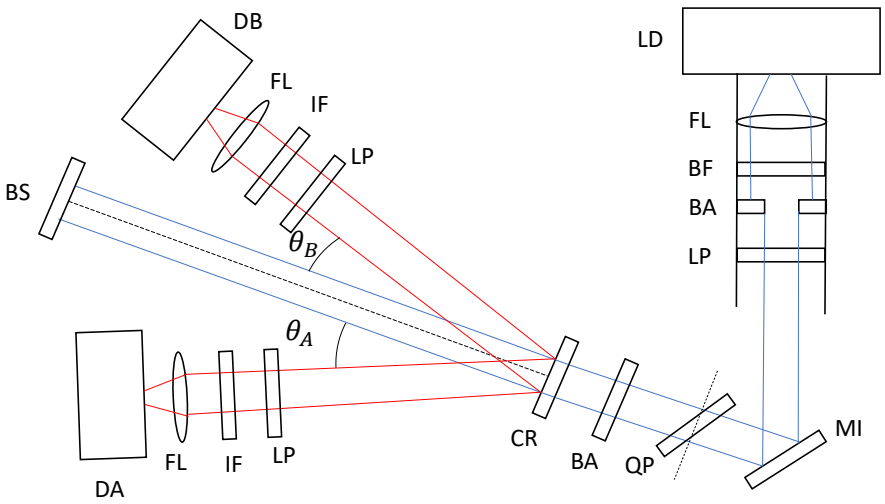

Figure 8: Schematic representation of the optical elements of the apparatus. LD: laser diode. FL: focusing lens. BF: blue filter. BA: beam aperture. LP: linear polarizer. MI: mirror. QP: quartz plate, tilted with respect to the beam trajectory. CR: set of BBO crystals. IF: infrared filter. DA: detector A. DB: detector B. BS: beam stop.

2.2 Mechanics

Since the downconverted photons exit the BBO crystals in a small aperture angle cone, the aligning of the systems is hard to make in the discrete matrix of holes of an optical breadboard or table. For that reason, we designed and constructed a series of elements to easily align the components. All the pieces were designed using Autodesk Fusion 360. Sketches can be found in Appendix B.

Central arm: the central arm consists of an anchor-like piece with a 25 mm diameter hole in the middle that allows it to rotate around a standard ∅25 mm post holder. One end of the arm is a rounded bar designed to fit inside of a 66 mm double dovetail rail, allowing to mount the desired optical elements over a rail and then rotate them freely without realigning them. The other end consists of an arc with notches every 0.5°. This is used as a goniometer to align the detection systems. See Fig. 13.

Rotation arm: the rotation arm consists of a 685 mm bar with a ∅25 mm hole in one end to pivot around the same post holder. The other end is also designed to fit inside a 66 mm double dovetail rail. The length of the bar is such that the two detection branches can be aligned in angles as small as 2°. This angle is limited by the finite width of the rails. The rotation arm is designed so that it can be rotated 180° around its length axis and be used in the second branch of the detection system. See Fig. 14.

The thickness of the central arm and the rotation arms are chosen so that when they are stacked on top of each other the optical rails lay flat on the breadboard and slide over it. This three-piece setup also provides a way of exploring the behavior of the coincidence and single counts profile for each angle. Furthermore, despite the covering box limiting the angles achievable in this particular setup, these pieces can be used to test many different entangled photon sources as long as they can be mounted on standard optical equipment.

Detector support plate: to hold the detectors vertically, we designed a 114 × 200 × 10 mm plate with a matrix of taped holes to screw the detectors using M3.5 screws. The distribution of the holes is such that the detectors can be fixed at four possible heights, each one 7 mm higher than the previous one. At the bottom of the plate, there are two ∅6 mm holes and two ∅3 mm holes to attach this plate to the rail support using both screws and dowel pins for a firmer hold. See Fig. 15.

Rail support: the rail support is a 114 mm long piece designed to attach the detector support plate to the optical rails. The bottom part has the same profile as a 66 mm taped dovetail so that it can be directly attached to the rails using 66 mm rail clamps. The top part is asymmetrical so that the active area of the SPCMs is aligned in the middle of the optical rail. The extruded part of the top side has two M6 screw holes and two ∅3 mm holes for the dowel pins. See Fig. 16.

2.3 Electronics

To consider a detection to be valid, we need to be able to confirm that both photons were produced and arrived at the same time. This helps eliminate unwanted detections produced by the background. For that reason, a coincidence circuit was developed following the design in Ref. [DM02a] shown in Fig. 9(a). The circuit is build on a printed circuit board and makes use of two 74ACT74 dual D-type positive edge-triggered flip-flops, two 51 Ω and three 1 kΩ resistors and three 220 pF capacitors. The components were added and welded to the printed circuit board. The readout of the circuit is recorded and processed with a Python program. The circuit and the programs needed to control it were developed by a previous student Martí Pedemonte. The circuit has a coincidence window of 2.5 ns, which is roughly the duration of the pulse generated by a detection of the SPDC modules.

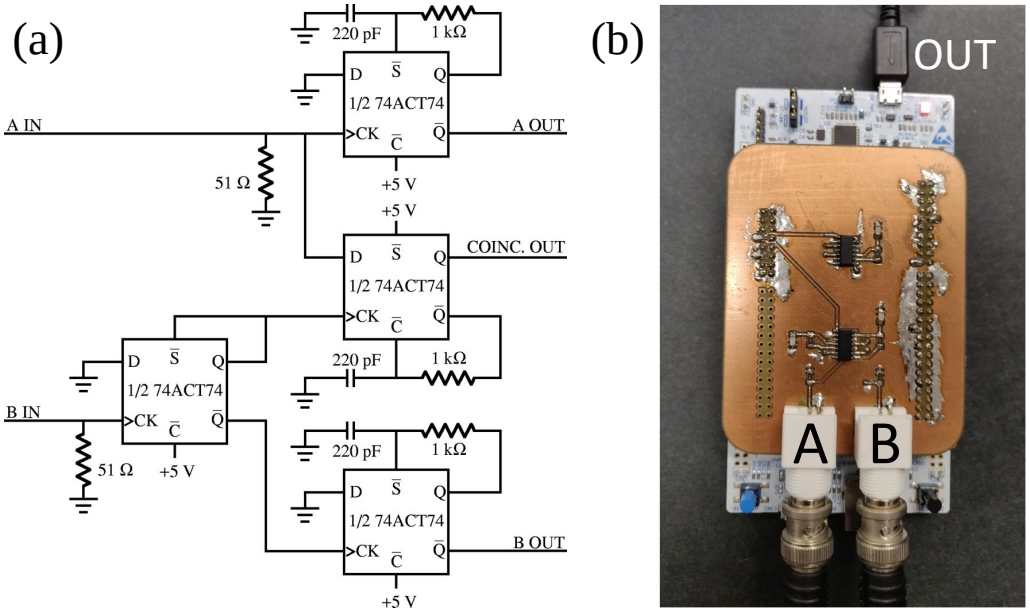

Figure 9: Coincidence circuit. (a): Schematic of the circuit from Ref. [DM02a]. (b): Final implementation of the coincidence circuit.

2.4 Mounting and aligning

We cut a 1 m rail into two 30 cm pieces and one 10 cm piece and drilled four M3 holes on the sides. The rotation arms were inserted in the 30 cm pieces and the central arm was inserted in the 10 cm piece. Then, all the rails were secured with 3 mm M3 grub screws. Having four holes allows for better aligning of the rails. A ∅25 mm post holder acts as a pivot axis for the three arms. This post holder holds the BBO crystals. To mount the optical components in the rails, we placed ∅12.7 mm post holders on top of 20 mm mounting platforms and fixed these to the rails using 20 mm double dovetail clamps. The optical components were mounted in optical posts.

The laser diode casing is mounted directly on the optical breadboard. The focusing lens, the blue filter, the iris diaphragm and the polarizer are mounted on the cage system attached to the casing. The mirror, the crystal and the iris diaphragm − which acts as a beam aperture − are mounted on the central arm rail.

The infrared filters are mounted on a Ø1" adjustable lens tube threaded into the rotation mount that holds the polarizer. Finally, the detectors are fixed to the detector support plate with M3.5 screws. The aluminum lens mount tubes in conjunction with the adjustable lens tube enclose the path of the photons between the polarizer and the detector active area, reducing the noise by one order of magnitude.

To align the system and obtain the maximum angular span, first we fixed one of the rails to the breadboard. Then, we aligned the center of the goniometer with a mark on the center of the rotation arm and fixed it. Then we rotated this arm and fixed it at 3.5° from the center of the goniometer. Finally, we rotated the central arm to align it with the rotation arm. The height of the diode casing was set by directing the beam to the active area of the detector. To make sure the incident beam was properly aligned, we positioned one closed iris diaphragm after the mirror and one at the tip of the rail of the fixed rotation arm. When the beam goes through both irises, the beam is well aligned. We can align the beam by rotating both the mirror and the diode casing.

3 Calibration and Test

3.1 Counts profile

We measured the number of counts in a single SPCM for the whole range of angles available. This experiment was performed using detector A and the bandpass filter, which blocks more stray light considering we expect to find photons of a wavelength of 810 nm. The polarizer was removed to let any possible down-converted photons in − when the BBO crystals were placed in the system − regardless of their polarization.

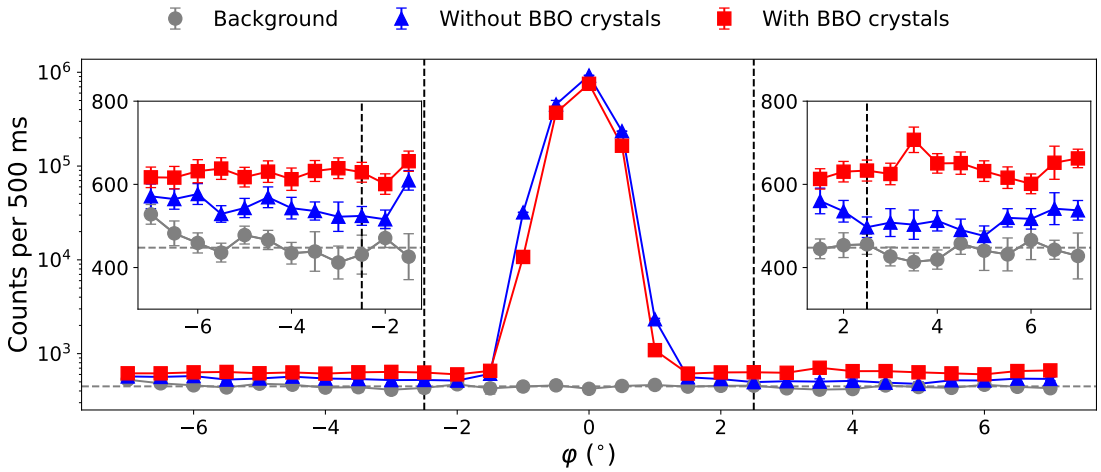

Figure 10: Counts per 500 ms at an angle φ from the beam. Grey circles correspond to the background (i.e. laser off). Blue triangles corresponds to the counts with the BBO crystal dismounted. Red squares correspond to the counts with the BBO crystal mounted. Error bars correspond to ± 1 standard deviation. The subplots left and right of the main plot show the [-7,-1.5] and [1.5,7] ranges. Vertical black dashed lines mark the optimal position $\varphi = \pm 2.5°$. Horizontal grey dashed line marks the background average.

The experiment was performed by making repeated sets of counts over a period of 500 ms. The total capture time for each experimental point was 250 s. We observe that in front of the beam, the number of counts naturally ascends to $\sim 10^6$ counts per 500 ms even with the filter on, with or without the crystals. Close to the center, the number of counts with the crystal on stays below the number of counts without the crystals. This is due to reflections and dispersion in the crystals. As we move away from the center, this reverses, showing more counts with the crystal. This can be due to (1) the detection of dispersed blue light from the laser or (2) the detection of down-converted infrared photons. Since the number of counts is very low, we cannot observe this light using an infrared laser viewing card, so we cannot discriminate between these two options visually. We do not see any different behavior around $\varphi = 2.5°$. This could be explained by considering that SPDC does not only produce photons at θ_{wo}, but at other angles too [DM02b]. These photons have different wavelengths than the target 810 nm, but a filter with a wide enough band could let these photons through. To find the optimal angular position of the detectors, similar experiments [DM02a, DM02b] perform an analysis of the coincidences by fixing the position of detector A and scanning the rest of the angles available for detector B. However, due to the compact nature of our experiment, we could not perform that kind of analysis. For that reason, we decided to follow the instructions of the crystal's manufacturer and place the detectors at $\theta_A = \theta_B = 2.5°$.

3.2 Dependency with Laser Power

Parametric Down-Conversion's efficiency lies around 10^{-6} [BLCB16]. For that reason we study the dependence of the number of counts and coincidences with the power of the incident laser beam. We measured the power of the laser at the position of the BBO crystals using a wavelength tunable power meter, see Fig. 11. The accidental coincidences are also represented. The number of accidental coincidences is computed as $N_{acc} = \frac{N_A N_B \tau}{T}$ [DM02a], where N_A and N_B are the individual counts of detectors A and B, τ is the coincidence window of 25 ns programmed in the circuit and T is the total acquisition time, which is 200 s.

We see a linear behavior for all the magnitudes measured. The number of total coincidences $N_{tot} = N_c - N_{acc}$ grows linearly as well, leading us to believe that higher powers of the laser could yield better results, as more photons interact with the crystal.

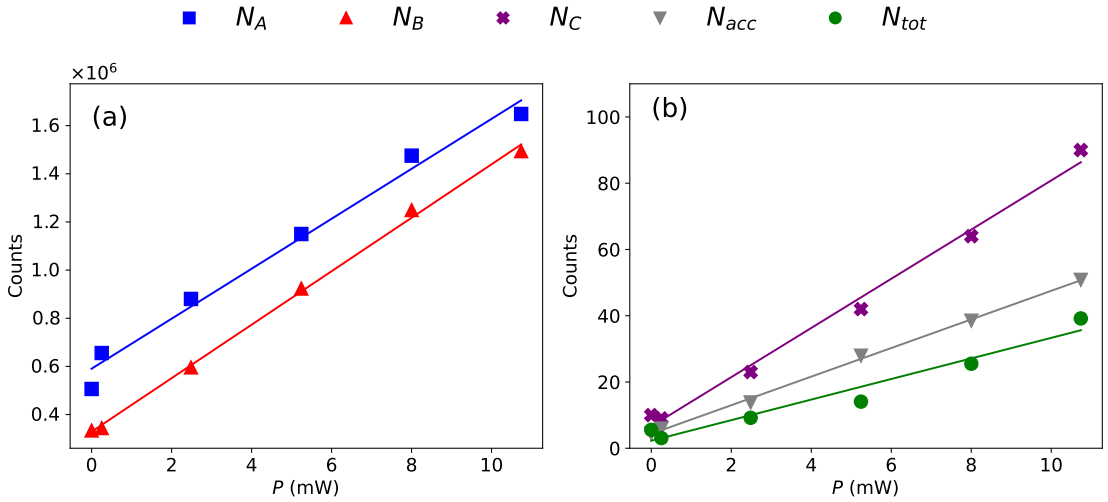

Figure 11: Number of counts as a function of the pump beam power. The represented lines are linear fits to the experimental data. (a): Individual detections of detectors A (blue squares, $R^2 = 0.98$) and B (red triangles, $R^2 = 0.998$). (b): Coincidences (purple crosses, $R^2 = 0.991$), accidental coincidences (grey inverted triangles, $R^2 = 0.998$) and total coincidences (green circles, $R^2 = 0.951$).

3.3 Validating the produced state. Measure of S

A procedure to properly tune the state is given in Ref. [DM02b]. However, given the low efficiency of our system and the absence of a goniometer on the mount of the quartz plate, this tuning was not possible. We decided to rotate the quartz plate roughly 25°, close to what is indicated in the mentioned paper. We will see that the disagreement between the results obtained and the theory cannot be explained by the wrong positioning of the quartz plate.

To compare the experimental results with the theory, we performed a series of measurements of the number of coincidences as a function of the angles of the polarizers. For that, we chose four values of $\alpha = -45°, 0°, 45°, 90°$ which coincide with the values needed to compute S and scanned β from 0° to 180°. The number of coincidences should have a behavior of the form

$$N_C(\alpha, \beta) = N_G\, p(\alpha, \beta) + N_0, \tag{32}$$

where N_G is the number of generated pairs, $p(\alpha, \beta)$ is the probability of coincidence detection given by Eq. (17) and N_0 is a correction factor needed to account for the coincidences detected at $\alpha = 0$, $\beta = 90$. Fig. 12 shows the experimental data for $\alpha = -45°, 0°, 45°, 90°$ compared with the theoretical prediction of the probability of coincidence given by Eq. (17) for various values of the relative phase ϕ. We find great discrepancy in the four cases. We can see that a variation in the relative phase cannot explain the discrepancy observed, since the data does not approximate any of the represented curves. The measured coincident photons do not seem to be entangled, at least not in the way we think.

The data obtained in the previous experiment allows the computation of S. The values are shown in Table 1. The value of S we obtain is

$$S = -0.2 \pm 0.2, \tag{33}$$

where the uncertainty in S is computed by propagation of errors from the uncertainty in the measures of coincidences. The value is far away from a violation of Bell's inequality. This is a confirmation of the absence of entangled photons. Since we observe an increase in detections when the BBO is present, we can conclude that the light we are measuring is dispersed and stray light. We can confirm that the efficiency of our experiment is not high enough to overcome the effects of noise.

Considering this disagreement with the theory, we decided to review the material and found that the BBO crystals we used were not adequate. As mentioned in Sec. 1.4, the efficiency of SPDC depends on the angle cut of the crystal. The optimal angle cut for a wavelength of 450 nm is around 29.2°, which is far from the 44.3° angle of our crystals. Furthermore, for the crystals to be indistinguishable, they need to be in optical contact, which our crystals were not. The results obtained are reasonable under these conditions.

α (°)	β (°)	$\overline{N}_A$	$\overline{N}_B$	N	N_{acc}	N_{tot}	ΔN_{tot}
-45	-22.5	367.80	750.24	65.01	52.41	12.59	3.45
-45	22.5	326.72	728.87	52.03	45.00	7.00	4.30
-45	67.5	363.23	1156.29	109.45	79.80	29.20	10.30
-45	112.5	397.33	1485.76	174.8	107.88	66.92	5.60
0	-22.5	460.33	1272.11	146.13	111.26	34.74	5.70
0	22.5	320.59	751.14	63.25	45.75	17.25	3.40
0	67.5	387.70	1272.60	125.54	93.72	31.28	7.81
0	112.5	397.33	1485.76	174.8	107.88	66.92	10.25
45	-22.5	339.40	817.78	66.12	52.74	13.26	1.34
45	22.5	369.24	873.62	87.13	61.30	26.70	5.67
45	67.5	385.69	1195.34	101.12	87.60	14.40	2.13
45	112.5	337.77	1299.61	113.63	84.34	28.66	1.34
90	-22.5	334.59	1054.58	83.12	67.05	16.95	2.34
90	22.5	343.05	661.72	61.35	43.14	18.86	5.34
90	67.5	525.40	1628.30	203.32	162.59	40.41	5.34
90	112.5	359.43	1257.58	103.17	85.90	17.10	5.15

Table 1: Data obtained for the computation of S. $\overline{N}_A$ and $\overline{N}_B$ correspond to the average number of counts over 500 ms. The error in N_{tot} corresponds to 1 standard deviation. The acquisition time for each measure is $T = 1900$ s, and three iterations were made for each pair of angles.

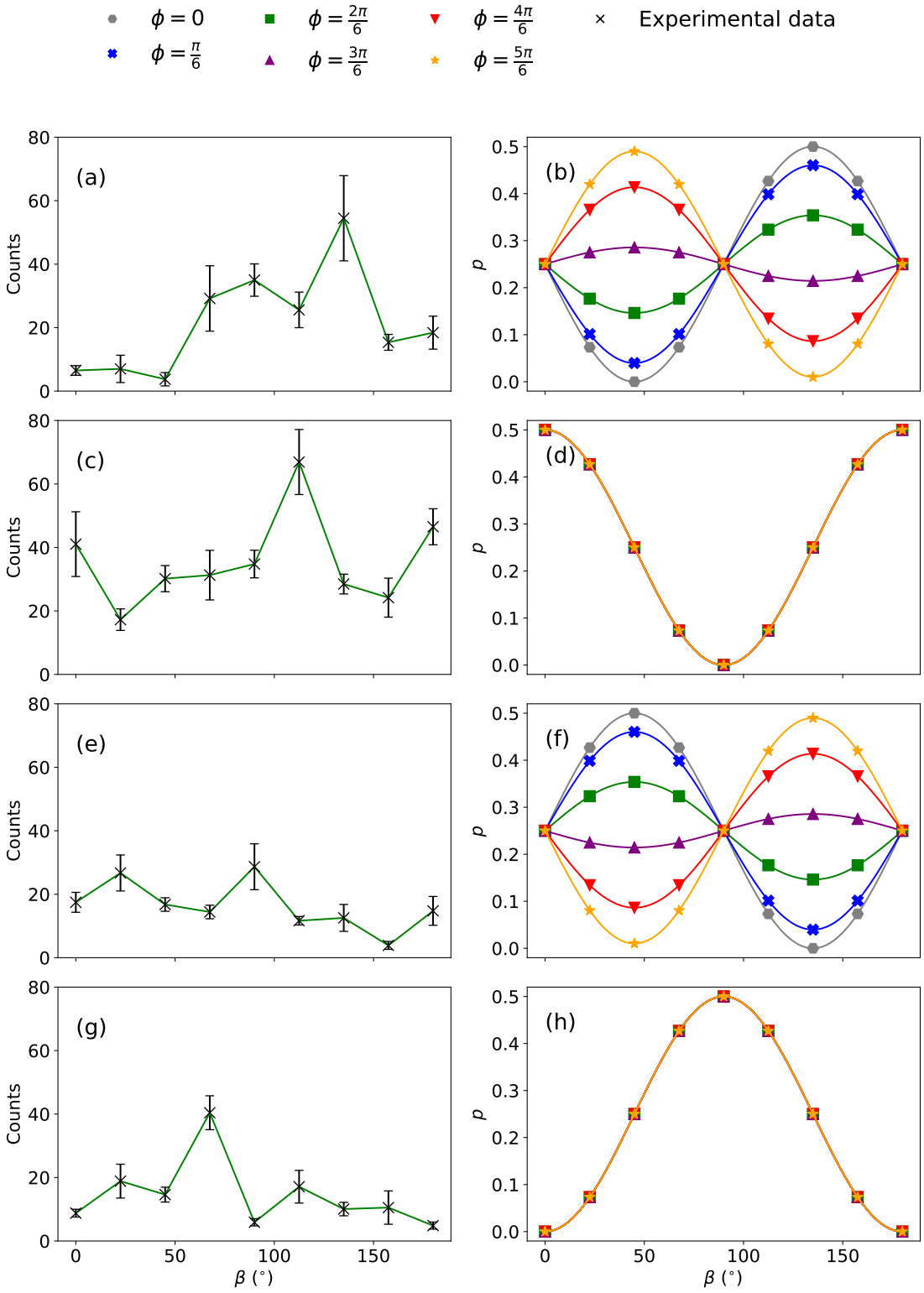

Figure 12: Coincidences and probability of coincidence as a function of the angle of polarizer β for different values of α. (a) and (b): $\alpha = -45°$. (c) and (d): $\alpha = 0°$. (e) and (f) $\alpha = 45°$. (g) and (h): $\alpha = 90°$. Measurement of experimental points in (a), (c), (e) and (g) were performed with a capture time $T = 1900$ s and averaged over 3 sets of measurements. Error bars correspond to 1 standard deviation. Different curves of figures (b), (d), (f) and (h) show the values for different values of the relative phase ϕ between 0 and π.

4 Conclusions

We have built, characterized and performed a Bell test in a compact, portable system. The mechanics and electronics developed proved to be effective for the experiments performed. The reported value $S = -0.2 \pm 0.2$ is reasonable considering that the photons we are detecting seem not to be in the desired state. We are led to believe that the detections are purely due to stray light and electronic noise of the detectors and coincidence circuit. Finer adjustment of the other parameters of the experiment, such as the distance between the lenses and the detectors and the angle of the quartz plate, as well as faster experiments are needed to be able to tune the Quantum state of the photons.

We have studied the theory behind the apparatus, including the CHSH Bell's inequality and Spontaneous Parametric Down-Conversion to perform a Bell test experimentally. We have reviewed a Hidden Variable Theory and compared it to the predictions of Quantum Theory, finding an incompatibility between the two throughout the whole angular spectrum.

Due to long manufacture and shipping times, we could not substitute the BBO crystals in time for this thesis. Independently from the specific source of entangled photons, the apparatus allows testing polarization-entangled infrared-photons of any kind, which has great applications in fields such as Quantum Information Theory and Quantum Cryptography. We expect that by changing the crystals, the apparatus should be able to obtain a violation of Bell's inequality. Higher efficiencies will lead to shorter experiments such as the ones described in Refs. [KWW+99, DM02a, DM02b].

Bibliography

[ABB+18] A. Acín, I. Bloch, H. Buhrman, T. Calarco, C. Eichler, J. Eisert, D. Esteve, N. Gisin, S. J. Glaser, F. Jelezko, S. Kuhr, M. Lewenstein, M. F. Riedel, P. O. Schmidt, R. Thew, A. Wallraff, I. Walmsley, and F. K. Wilhelm. The quantum technologies roadmap: a european community view. *New Journal of Physics*, 20(8):080201, 2018.

[BCP+14] N. Brunner, D. Cavalcanti, S. Pironio, V. Scarani, and S. Wehner. Bell nonlocality. *Reviews of Modern Physics*, 86(2):419–478, 2014.

[Bel64] J. S. Bell. On the einstein-podolsky-rosen paradox. *Physics*, 1:195–200, 1964.

[BLCB16] M. Bock, A. Lenhard, C. Chunnilall, and C. Becher. Highly efficient heralded single-photon source for telecom wavelengths based on a ppln waveguide. *Optics Express*, 24(21):23992–24001, 2016.

[Boy08] R. W. Boyd. *Nonlinear Optics (3rd edition)*. Academic Press, 2008.

[CHSH69] J. F. Clauser, M. A. Horne, A. Shimony, and R. A. Holt. Proposed experiment to test local hidden-variable theories. *Phys. Rev. Lett.*, 23:880–884, 1969.

[Cir80] B. S. Cirel'son. Quantum generalizations of bell's inequality. *Letters in Mathematical Physics*, 4:93–100, 1980.

[DM02a] D. Dehlinger and M. W. Mitchell. Entangled photon apparatus for the undergraduate laboratory. *American Journal of Physics*, 70(9):898–902, 2002.

[DM02b] D. Dehlinger and M. W. Mitchell. Entangled photons, nonlocality, and bell inequalities in the undergraduate laboratory. *American Journal of Physics*, 70(9):903–910, 2002.

[Ein05] A. Einstein. On a heuristic viewpoint concerning the production and transformation of light. *Annalen der Physik*, 17:132–148, 1905.

[EPR35] A. Einstein, B. Podolsky, and N. Rosen. Can quantum-mechanical description of physical reality be considered complete? *Phys. Rev.*, 47:777–780, 1935.

[KWW+99] P. G. Kwiat, E. Waks, A. G. White, I. Appelbaum, and P. H. Eberhard. Ultrabright source of polarization-entangled photons. *Physical Review A*, 60:R773–R776, 1999.

[Pla00] M. Planck. On the theory of the energy distribution law of the normal spectrum. *Verhandl. Dtsch. phys. Ges*, 2, 1900.

A Material list

ITEM	**SUPPLIER**	**CODE**	#
B Pin Code Laser Diode	Thorlabs	DL5146-101S	1
Laser Diode Socket for Ø5.6 mm Laser, 3 Pin	Thorlabs	S7060R	1
Laser Diode Starter Set	Thorlabs	LTC56A/M	1
Benchtop Laser Diode/TEC Controller, 1 A / 96 W	Thorlabs	ITC4001	1
Connection Cable for LDC4000/ITC4000, 13W3 to D-Sub-9, 5 A	Thorlabs	CAB4005	1
Connection Cable for TED4000/ITC4000, 17W2 to D-Sub-9, 5 A	Thorlabs	CAB4000	1
Connection Cable for TED4000/ITC4000, 17W2 to D-Sub-9, 5 A	Thorlabs	CAB4000	1
Cage Assembly Rod, 4" Long, Ø6 mm	Thorlabs	ER4	4
Mounted Aspheric Lens	Thorlabs	C230TMD-A	1
16 mm Cage Plate for Ø11 mm Optic, 2 SM11RR Retaining Rings Included	Thorlabs	SP13	1
SCHOTT BG-25 (UV-VIS), 25.4mm Dia., Colored Glass Bandpass Filter	Edmund Optics	84-901	1
30 mm Cage System Iris Diaphragm (Ø0.8 - Ø20 mm)	Thorlabs	CP20D	1
30mm Dia. High Performance Glass Linear Polarizer	Edmund Optics	49-078	1
Cage Rotation Mount for Ø1" Optics, SM1 Threaded, 8-32 Tap	Thorlabs	CRM1	1
Quartz single crystal, X-cut, 10x10x0.5mm, 2SP	MTI Corporation	SOX101005S2	1
Ø1" Broadband Dielectric Mirror, 400 - 750 nm	Thorlabs	BB1-E02	1
Fixed Ø1" Mirror Mount, M4 Tap	Thorlabs	FMP1/M	1
Mounted Standard Iris, Ø25 mm Max Aperture, TR75/M Post	Thorlabs	ID25/M	1

6 x 6 x 0.2mm, 800nm THG, Type I BBO Nonlinear Crystal	Edmund Optics	11-170	2
Rotation Mount for ⌀1"	Thorlabs	RSP1	3
Ø1" Linear Polarizer with N-BK7 Windows, 600-1100 nm	Thorlabs	LPNIRE100-B	2
Ø1" Adjustable Lens Tube, 0.81" Travel Range	Thorlabs	SM1V10	2
SCHOTT RG-780, 25.4mm Dia., Longpass Filter	Edmund Optics	32-757	1
SPCM-AQR-12	PerkinElmer	N/A	2
Compact Variable Height Clamp, M6 Tapped, 5 Pack	Thorlabs	CL3/M-P5	2
Ø12.7 mm Post Holder, Spring-Loaded Hex-Locking Thumbscrew, L=50 mm, 5 Pack	Thorlabs	PH50/M-P5	1
Ø12.7 mm Post Holder with Hex-Locking Thumbscrew, L = 75 mm, Vacuum Compatible	Thorlabs	PH75V/M	1
M6 Tapped Dovetail for 66 mm Rails, 20 mm Long	Thorlabs	XT66DM1	8
20 mm Long Double Dovetail Clamp for 66 mm Rails	Thorlabs	XT66C1	10
66 mm Double Dovetail Rail, L = 1000 mm	Thorlabs	XT66DP-1000	1
Ø12.7 mm Optical Post, SS, M4 Setscrew, M6 Tap, L = 100 mm	Thorlabs	TR100/M	5
Analog Power Console, Si Sensor, 200 nm - 1100 nm, 50 nW - 50 mW	Thorlabs	PM120VA	1

B Pieces sketches

Central arm.

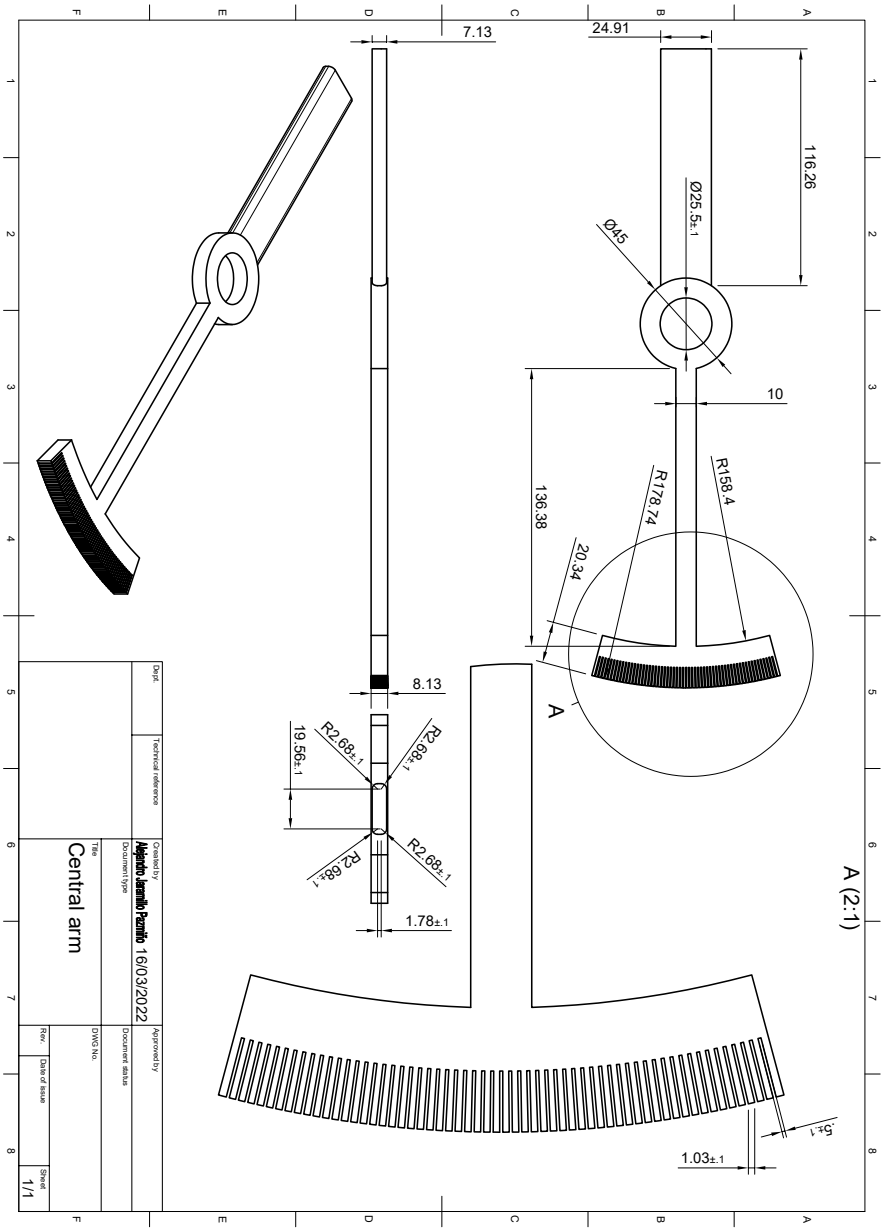

Figure 13: Central arm sketch.

Rotation arm.

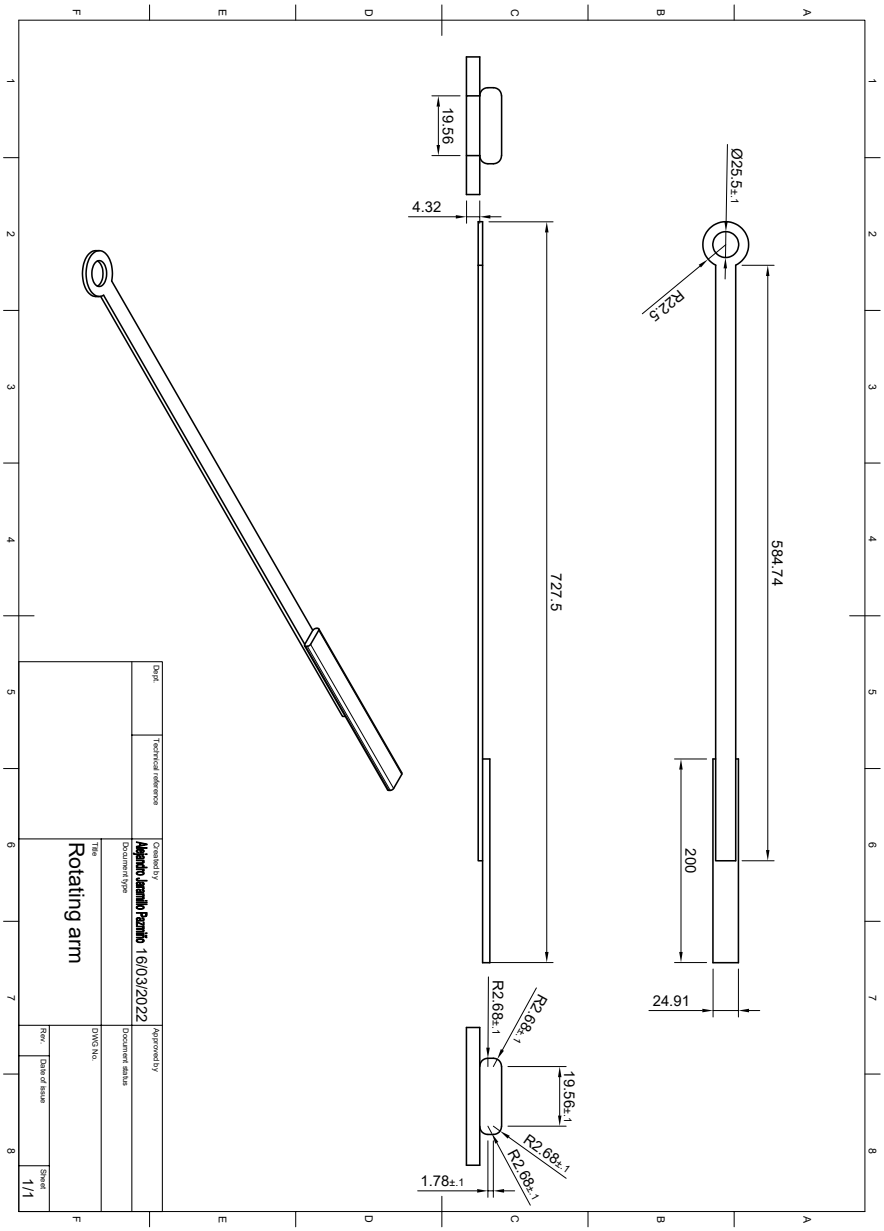

Figure 14: Rotation arm sketch

Detector support plate.

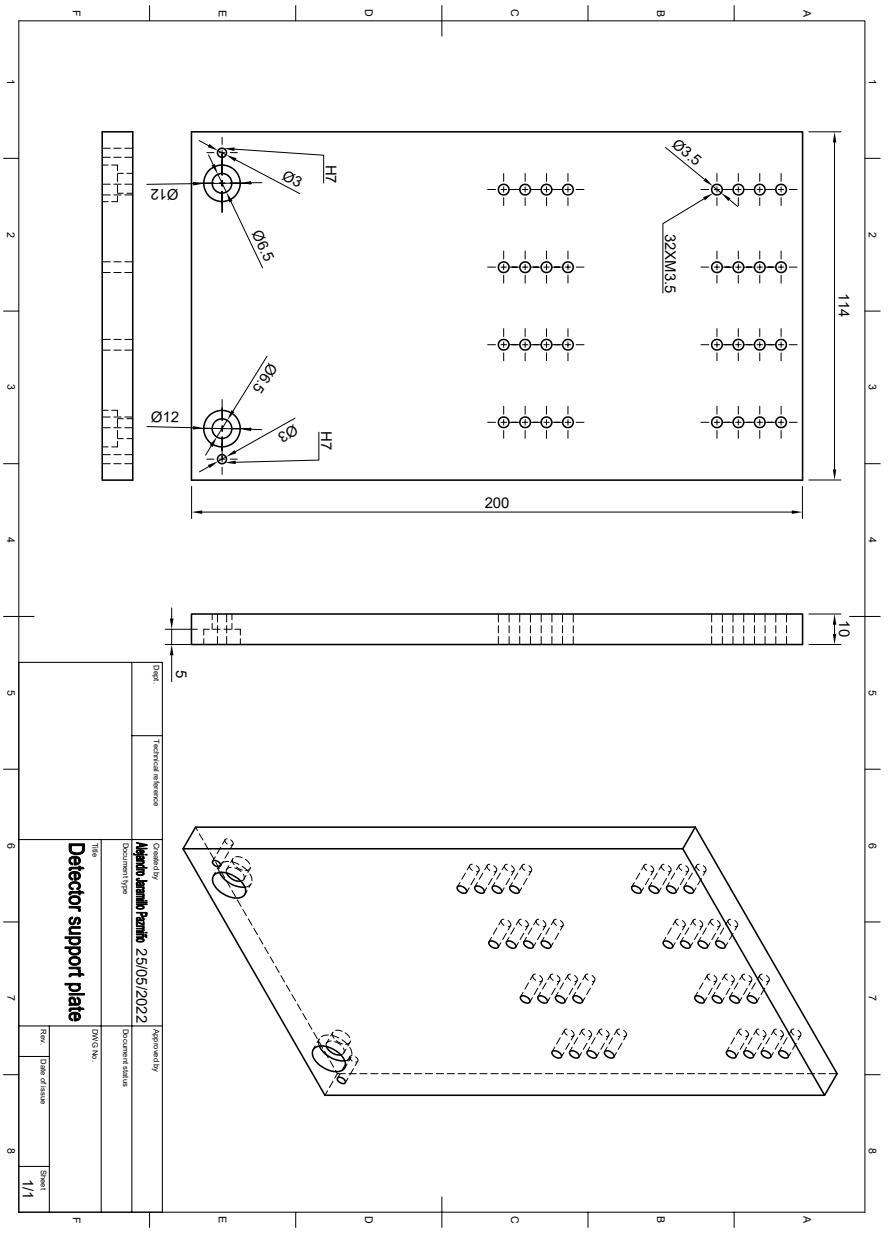

Figure 15: Detector support plate sketch.

Rail support.

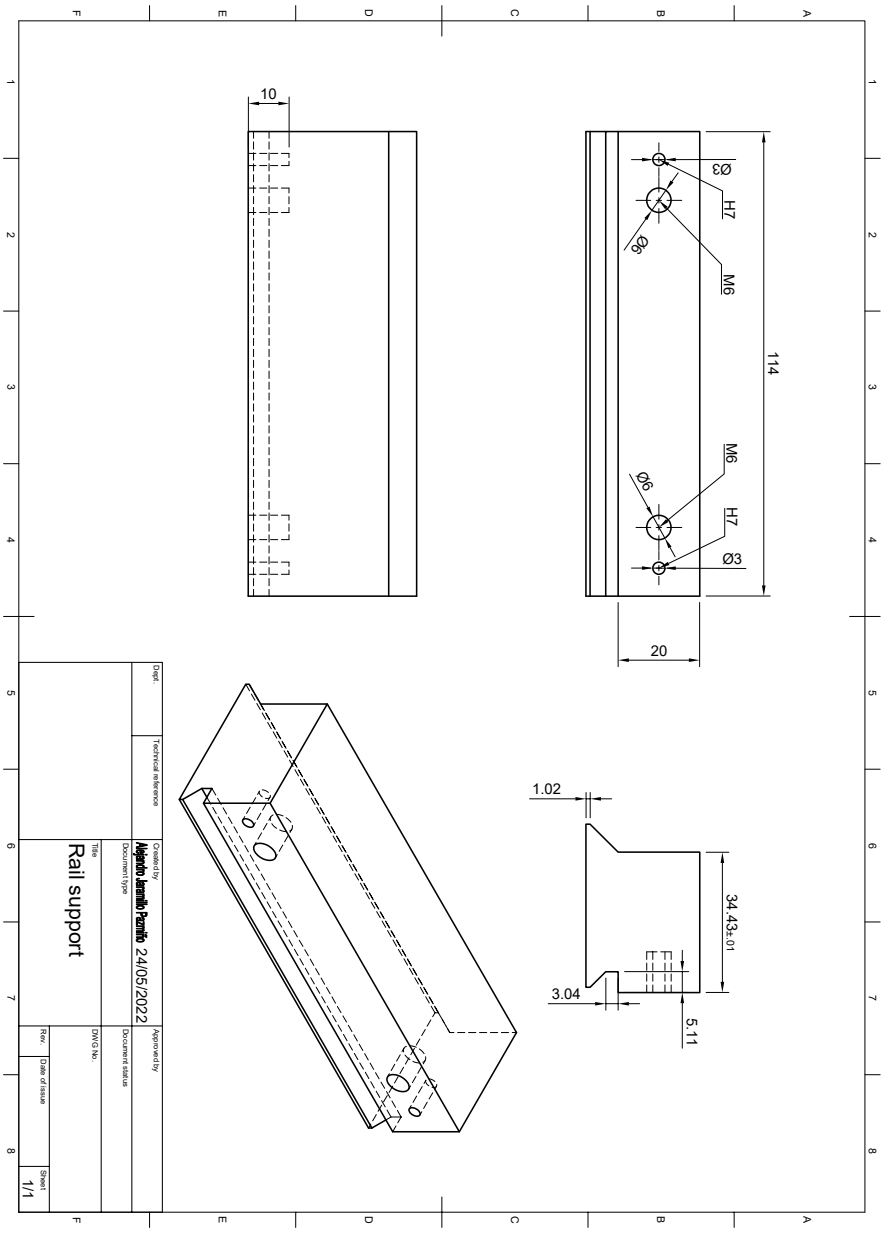

Figure 16: Rail support sketch.

C Hidden Variable Theory simulation code

```
pip install qutip
from qutip import *
import numpy as np
import matplotlib.pyplot as plt
import random as rnd

def probs(a,b,nfot):
# Function that computes the probabilities for each configuration
using booleans
    gamma = np.random.rand(nfot)*2*np.pi
    closertosmallA = abs(gamma-a) <= np.pi/4
    closertobigA = (abs(gamma-a) > 3*np.pi/4)*(abs(gamma-a) <= 5*np.pi/4)
    closertoBiggA = abs(gamma-a) >= 9*np.pi/4
    closertoA = closertosmallA+closertobigA+closertoBiggA

    closertosmallB = abs(gamma-b) <= np.pi/4
    closertobigB = (abs(gamma-b) > 3*np.pi/4)*(abs(gamma-b) <= 5*np.pi/4)
    closertoBiggB = abs(gamma-b) >= 9*np.pi/4
    closertoB = closertosmallB+closertobigB+closertoBiggB

    #print(closertoB)
    #print(1-closertoB)

    probs = np.array([np.count_nonzero(closertoA*closertoB),
    np.count_nonzero(closertoA*(1-closertoB)),
    np.count_nonzero((1-closertoA)*closertoB),
    np.count_nonzero((1-closertoA)*(1-closertoB))])/nfot

    return probs

def Eopt(a,b,nfot):
# Expectation value
    return probs(a,b,nfot)[0]+probs(a,b,nfot)[3]-probs(a,b,nfot)[1]
    -probs(a,b,nfot)[2]

def S(a1,a2,b1,b2,nfot):
    return Eopt(a1,b1,nfot)+Eopt(a1,b2,nfot)+Eopt(a2,b1,nfot)
    -Eopt(a2,b2,nfot)

# Number of photons we will use
nfot = 500000

# Angles
a1 = rad(0)
a2 = rad(45)
b1 = rad(22.5)
```

```
# Number of points that will be computed
ndot = 200
b2 = np.linspace(0,np.pi,ndot)

Sval = 0.0*b2
pvv = 0.0*b2

for i in range(ndot):
    Sval[i] = S(a1,a2,b1,b2[i],nfot)

# QUANTUM

state = 1/np.sqrt(2)*(tensor(basis(2,0),basis(2,0))+
tensor(basis(2,1),basis(2,1)))
A1 = sigmax()*np.cos(a1*2)+sigmaz()*np.sin(a1*2)
A2 = sigmax()*np.cos(a2*2)+sigmaz()*np.sin(a2*2)
B1 = sigmax()*np.cos(b1*2)+sigmaz()*np.sin(b1*2)

beta = np.linspace(0 ,2*np.pi,ndot)


Squant = np.array([0.0]*ndot)

for i in range(ndot):
    B2 = np.cos(2*b2[i])*sigmax()+np.sin(2*b2[i])*sigmaz()
    Spre = state.dag()*(tensor(A1,B1)+tensor(A1,B2)+tensor(A2,B1)-
    tensor(A2, B2))*state
    Squant[i] = np.real(Spre[0][0][0])
```